The physics of pulses in gamma-ray bursts: emission processes, temporal profiles and time-lags

Frédéric Daigne, Robert Mochkovitch

Mon. Not. R. Astron. Soc. **342,** 587–592 (2003)

The physics of pulses in gamma-ray bursts: emission processes, temporal profiles and time-lags

Frédéric Daigne★ and Robert Mochkovitch
Institut d'Astrophysique de Paris, 98 bis bd Arago, 75014 Paris, France

Accepted 2003 February 21. Received 2002 December 12

ABSTRACT

We present a simple, semi-analytical model to explain gamma-ray burst temporal and spectral properties in the context of the internal shock model. Each individual pulse in the temporal profiles is produced by the deceleration of fast moving material by a comparatively slower layer within a relativistic wind. The spectral evolution of synthetic pulses is first obtained with standard equipartition assumptions to estimate the post-shock magnetic field and the electron Lorentz factor. We find $E_{\rm p} \propto t^{-\delta}$ with $\delta = 7/2$, which is much steeper than the observed slopes $\delta_{\rm obs} \lesssim 1.5$. We therefore consider the possibility that the equipartition parameters depend on the shock strength and post-shock density. We then obtain a much better agreement with the observations and our synthetic pulses satisfy both the hardness–intensity and hardness–fluence correlations. We also compute time-lags between profiles in different energy channels and we find that they decrease with increasing hardness. Finally, we compare our predicted time-lag–luminosity relation with the result of Norris, Marani & Bonnell obtained from six bursts with known redshift.

Key words: hydrodynamics – radiation mechanisms: non-thermal – shock waves – gamma-rays: bursts.

1 INTRODUCTION

Cosmic gamma-ray burst (hereafter GRBs) exhibit a great diversity of duration and profiles. The distribution of durations is clearly bimodal with two peaks at approximately 0.2 and 20 s. GRB light curves are highly variable but can often be interpreted in terms of a succession of elementary pulses which possibly overlap (Norris et al. 1996). These pulses appear as the building blocks of the profiles and understanding their physical origin would certainly represent a clue towards a better description of the whole GRB phenomenon. The pulse temporal evolution has often been described by a fast rise followed by an exponential decay (the so-called FRED shape; see Fishman et al. 1994), but other mathematical behaviour such as stretched exponentials, Gaussian (Norris et al. 1996) or power-law decays (Ryde & Svensson 2000) have also been proposed. Spectral hardness decreases during pulse decay and two relations between the temporal and spectral properties, the hardness–intensity correlation (HIC; Golenetskii et al. 1983) and the hardness–fluence correlation (HFC; Liang & Kargatis 1996) appear to be satisfied by a substantial fraction of GRB pulses during the decay phase. Pulse profiles peak earlier in higher-energy bands and the corresponding time-lags between different energy channels correlate to pulse hardness and peak luminosity (Norris, Marani & Bonnell 2000). These observational results must be reproduced by the models and may help to discriminate among different possibilities.

Two distinct mechanisms have been proposed to explain the origin of pulses in GRBs. In the external shock model they are formed when a relativistic shell ejected by the central engine is decelerated by the circumstellar material (Meszaros & Rees 1993). An homogeneous medium leads to a single pulse but an irregular, clumpy environment can produce a complex profile if a large number of small clouds are present (Dermer & Mitman 1999). In the internal shock model (Rees & Meszaros 1994) the central engine generates a relativistic flow with a highly non-uniform distribution of the Lorentz factor and the pulses are made by collisions between rapid and slower parts of the flow. In the two scenarios the variability of the profiles has a very different interpretation. In one case it provides a 'tomography' of the burst environment while in the second case it reveals the activity of the central engine.

In this paper we consider in some detail the mechanism of pulse formation by internal shocks. Three characteristic time-scales may be relevant during pulse evolution: the time $t_{\rm rad}$ required to radiate the energy dissipated in shocks; the dynamical time $t_{\rm dyn}$, i.e. the time taken by internal shocks to travel throughout the flow and the angular spreading time $t_{\rm ang}$ corresponding to the delay in arrival time of photons emitted from a spherical shell. A short radiative time $t_{\rm rad} \ll t_{\rm dyn}, t_{\rm ang}$ appears to be mandatory to avoid adiabatic losses and to maintain sufficient efficiency. This condition is satisfied by the synchrotron process, which is the most commonly invoked

★E-mail: daigne@iap.fr

radiation mechanism in GRBs. If the thickness of colliding shells is small compared with their initial separation, $t_{\rm dyn} \ll t_{\rm ang}$ and the pulse temporal evolution is fixed by geometry; conversely if the source produces a continuous wind rather than a series of discrete, well-separated shells, $t_{\rm dyn} \gtrsim t_{\rm ang}$ and hydrodynamical effects control the pulse shape.

Pulse evolution has been studied extensively when it is dominated by geometry (see, e.g., Fenimore, Madras & Nayakshin 1996; Kobayashi, Piran & Sari 1997) but discrepancies between model predictions and the observations (Soderberg & Fenimore 2001) have cast some doubt concerning the validity of the internal shock model. Our purpose is to see if the situation can be improved when the hydrodynamical point of view is adopted. In Section 2 we summarize some basic information regarding pulse temporal and spectral evolution. We then develop, in Section 3, a simple model where pulses are formed when a fast moving wind is decelerated by a comparatively slower shell. Spectral evolution is considered in Section 4 where constraints are obtained on the GRB radiation mechanism. Temporal profiles computed with our model are presented in Section 5 and time-lags are discussed in Section 6. Section 7 gives our conclusions.

2 TEMPORAL AND SPECTRAL EVOLUTION DURING PULSE DECAY

We consider a pulse characterized by a photon flux $N(t)$ in the energy range (E_1, E_2), a peak energy $E_{\rm p}(t)$ of the $E^2\mathcal{N}(E,t)$ spectrum and a photon fluence defined by

$$\frac{{\rm d}\Phi_{\rm N}(t)}{{\rm d}t} = N(t) = \int_{E_1}^{E_2} \mathcal{N}(E,t)\,{\rm d}E. \tag{1}$$

The HIC and the HFC are then given by

$$E_{\rm p}(t) \propto N(t)^{\delta} \tag{2}$$

and

$$E_{\rm p}(t) \propto {\rm e}^{-a\Phi_{\rm N}(t)}, \tag{3}$$

where a is an exponential decay constant. For pulses satisfying both the HIC and the HFC, Ryde & Svensson (2000) have shown that the photon flux and the peak energy follow simple power laws during the decay phase

$$N(t) = \frac{N_0}{1+t/\tau} \tag{4}$$

and

$$E_{\rm p}(t) = \frac{E_{\rm p,0}}{(1+t/\tau)^{\delta}}, \tag{5}$$

where $t = 0$ corresponds to the maximum of $N(t)$.

Ryde & Svensson (2002) performed a detailed analysis of the decay behaviour of a sample of 25 long and bright pulses to check whether it was indeed described by equations (4) and (5). They found that to account for the temporal and spectral evolution of all the pulses, equation (4) had to be replaced by the more general expression

$$N(t) = \frac{N_0}{(1+t/\tau)^{n}}. \tag{6}$$

If $n \neq 1$, the δ indices appearing in equations (2) and (6) are different and following Ryde & Svensson (2002) we then write $E_{\rm p}(t) = E_{\rm p,0}/(1+t/\tau)^{\delta^\star}$ with $\delta^\star = n\delta$. Ryde & Svensson (2002) found that the distribution of n in their sample was sharply peaked at $n = 1$ with, however, a secondary bump at $n \lesssim 3$. The values of $\delta^\star$ were all smaller than 1.5 for the $n = 1$ pulses, but could reach 3.5 when $n \approx 3$. The distribution of δ was narrower with $0.5 \lesssim \delta \lesssim 1$ in most of the sample.

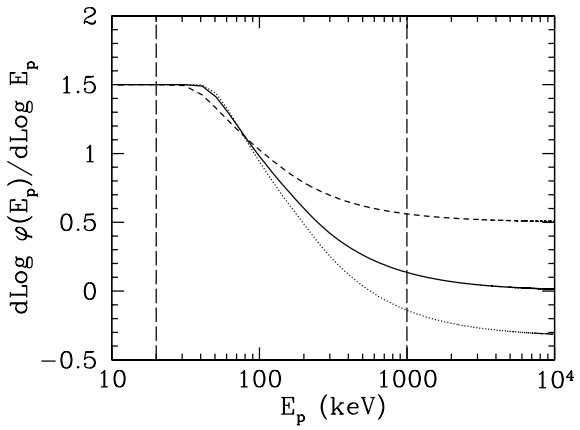

Figure 1. Derivative of $\varphi(E_{\rm p})$ for three Band functions with $\beta = -2.5$ and $\alpha = -2/3$ (dotted line) $\alpha = -1$ (full line) and $\alpha = -1.5$ (dashed line). The two vertical lines limit the BATSE spectral range. The average slope during pulse decay typically lies between 0 and 1.

Once the decay behaviour of $N(t)$ and $E_{\rm p}(t)$ has been specified, it becomes possible to obtain the evolution of the bolometric energy flux $F_{\rm E}(t)$ since

$$F_{\rm E}(t) = \int_0^{\infty} \mathcal{N}(E,t)E\,{\rm d}E = E_{\rm p}^2 \int_0^{\infty} \mathcal{N}(x,t)x\,{\rm d}x, \tag{7}$$

where $x = E/E_{\rm p}$. We suppose that the temporal and spectral behaviour can be separated in $\mathcal{N}(x,t)$:

$$\mathcal{N}(x,t) = A(t)\mathcal{B}(x), \tag{8}$$

with $\mathcal{B}(x)$ representing the spectrum shape. The photon flux in the energy range (E_1, E_2) is then given by

$$N(t) = \int_{E_1}^{E_2} \mathcal{N}(E,t)\,{\rm d}E = \frac{F_{\rm E}(t)\varphi(E_{\rm p})}{E_{\rm p}(t)\varphi_0}, \tag{9}$$

so that

$$F_{\rm E}(t) = N(t)E_{\rm p}(t)\frac{\varphi_0}{\varphi(E_{\rm p})} = \frac{N_0 E_{\rm p,0}}{(1+t/\tau)^{1+\delta_\star}}\frac{\varphi_0}{\varphi(E_{\rm p})} \tag{10}$$

with

$$\varphi(E_{\rm p}) = \int_{E_1/E_{\rm p}}^{E_2/E_{\rm p}} \mathcal{B}(x)\,{\rm d}x \tag{11}$$

and

$$\varphi_0 = \int_0^{\infty} x\mathcal{B}(x)\,{\rm d}x. \tag{12}$$

The derivative of $\varphi(E_{\rm p})$ has been represented in Fig. 1 for the BATSE spectral range (20, 1000 keV), using a standard Band function (Band et al. 1993) with low and high energy indices $\alpha = -\frac{2}{3}, -1$ or -1.5 and $\beta = -2.5$. At low (respectively, high) $E_{\rm p}$, $\varphi(E_{\rm p})$ is given by a simple power law $E_{\rm p}^{-(\beta+1)}$ [respectively, $E_{\rm p}^{-(\alpha+1)}$] but for intermediate values ($E_1 < E_{\rm p} < E_2$), which are representative of the decay phase in the Ryde & Svensson (2002) sample, $\varphi(E_{\rm p})$ does not have a simple analytical form. Assuming that it can still be approximated by a power law, $\varphi(E_{\rm p}) \propto E_{\rm p}^{-(\zeta+1)}$, where ζ is a weighted average of the low- and high-energy spectral indices ($-2 \lesssim \zeta \lesssim -1$) the bolometric energy flux also follows a power law:

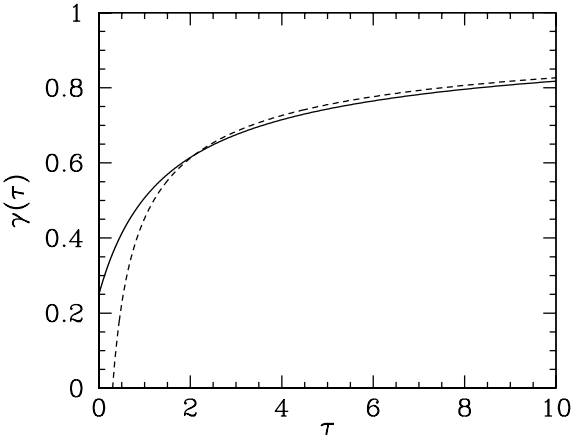

Figure 2. Solution for $\gamma(\tau)$ corresponding to equation (21) with $\gamma_0 = 0.25$. The dashed line is the approximation given by equation (23).

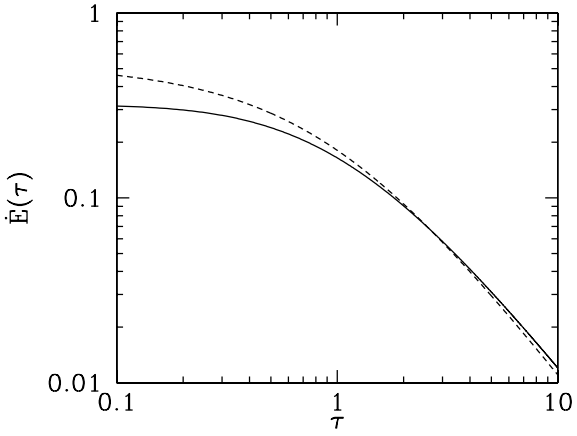

Figure 3. Dissipated power in units of $1/2\dot{M}\Gamma_1 c^2$ for our pulse model with $\gamma_0 = 0.25$. The dashed line corresponds to equation (24) while the full line takes into account angular spreading.

$$F_{\rm E}(t) \propto \frac{1}{(1+t/\tau)^{\epsilon}} \tag{13}$$

with

$$\epsilon = n + (2+\zeta)\delta_{\star}. \tag{14}$$

The slope of the HIC is then given by

$$\delta = \frac{\delta_{\star}}{n} = \frac{1}{\epsilon/\delta_{\star} - (2+\zeta)}. \tag{15}$$

If the temporal and spectral evolution during pulse decay is due to geometrical effects alone $\epsilon = 3$ and $\delta^{\star} = 1$ (Granot, Piran & Sari 1999), which leads to $\delta = 1/(1-\zeta)$. With $-2 \lesssim \zeta \lesssim -1$ the resulting value $0.3 \lesssim \delta \lesssim 0.5$ lies below what is found in most observed pulses (Soderberg & Fenimore 2001).

Geometrical effects govern pulse evolution if the shell thickness is small compared with their initial separation. However, if a continuous outflow emerges from the central engine the hydrodynamical time-scale can play a dominant role during pulse decay. We have then developed a simple model to check whether a better agreement can be found with the observations when the hydrodynamical aspect of the flow is taken into account.

3 A SIMPLE PULSE MODEL

We consider a relativistic wind where a slow shell of mass M_0 and Lorentz factor Γ_0 decelerates a more rapid part of the flow characterized by a constant mass flux $\dot{M}$ (in the source frame) and Lorentz factor $\Gamma_1 > \Gamma_0$. We do not solve the true hydrodynamical problem but rather approximate the flow evolution by considering that fast material is 'accreted' by the slow shell. The accretion rate is given by

$$\frac{{\rm d}M}{{\rm d}t} = \dot{M}(1-\gamma^2), \tag{16}$$

where t is the observer time and $\gamma = \Gamma/\Gamma_1$ (with Γ and M being the current Lorentz factor and mass of the slow shell). As a result of the accretion of fast moving material, the Lorentz factor of the slow shell increases. When a mass element ${\rm d}M$ is accreted the Lorentz factor becomes

$$\Gamma + {\rm d}\Gamma = \left(\Gamma_1\Gamma\frac{\Gamma_1\,{\rm d}M + \Gamma M}{\Gamma\,{\rm d}M + \Gamma_1 M}\right)^{1/2}, \tag{17}$$

so that

$$\frac{{\rm d}\gamma}{{\rm d}M} = \frac{1-\gamma^2}{2M}, \tag{18}$$

which can be integrated to give

$$\mu = \left(\frac{1+\gamma}{1-\gamma}\right) \Big/ \left(\frac{1+\gamma_0}{1-\gamma_0}\right), \tag{19}$$

where $\mu = M/M_0$ and $\gamma_0 = \Gamma_0/\Gamma_1$. Introducing $t_0 = M_0/\dot{M}$ and $\tau = t/t_0$, equations (16)–(19) yield

$$\frac{{\rm d}\gamma}{{\rm d}\tau} = Q(1-\gamma^2)(1-\gamma)^2 \tag{20}$$

with $Q = 1/2[(1+\gamma_0)/(1-\gamma_0)]$. Equation (20) has the analytical solution

$$\tau = \frac{1}{Q}\,[F(\gamma) - F(\gamma_0)], \tag{21}$$

where the function $F(\gamma)$ is given by

$$F(\gamma) = \frac{1}{8}\log\left(\frac{1+\gamma}{1-\gamma}\right) + \frac{1}{4(1-\gamma)} + \frac{1}{4(1-\gamma)^2}. \tag{22}$$

The solution $\gamma(\tau)$ corresponding to equation (21) has been represented in Fig. 2 for $\gamma_0 = 0.25$. When $\tau \gtrsim 2$, it is well approximated by

$$\gamma(\tau) \simeq 1 - \frac{1}{2\sqrt{Q\tau}}. \tag{23}$$

Once $\gamma(\tau)$ is known it is possible to calculate the dissipated power

$$\dot{\mathcal{E}}(\tau) = \frac{\dot{M}\Gamma_1 c^2}{2}(1-\gamma^2)(1-\gamma)^2, \tag{24}$$

which has been represented in Fig. 3. At large τ, it behaves as $\tau^{-3/2}$ since

$$\dot{\mathcal{E}}(\tau) \propto (1-\gamma)^3(1+\gamma) \propto \tau^{-3/2} \tag{25}$$

for $\tau \gtrsim 2$. Pulse evolution is essentially completed at $\tau \sim 10$ when $\Gamma/\Gamma_1 > 0.8$ and $\dot{\mathcal{E}}$ has decreased by more than an order of magnitude.

The dissipated power given by equation (24) is slightly different from what the observer will see since the energy released at time t is spread over an interval $\Delta\, t$ corresponding to the difference in arrival time for photons emitted by a shell of radius r moving at a Lorentz factor Γ,

$$\Delta t = \frac{r}{2c\Gamma^2}. \tag{26}$$

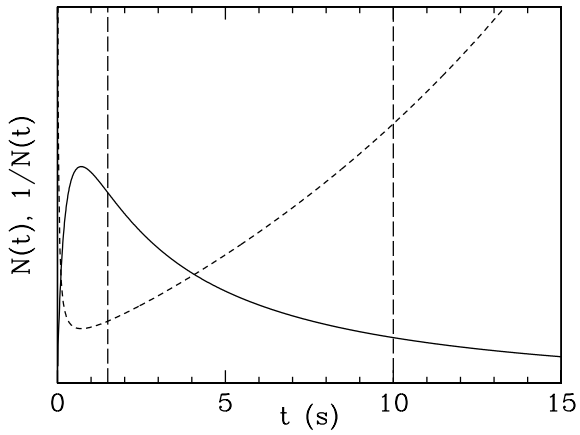

Figure 4. Pulse profile $N(t)$ (full line) and $1/N(t)$ (dashed line) produced by a relativistic outflow with $\Gamma_1 = 400$ decelerated by a slow shell of initial Lorentz factor $\Gamma_0 = 100$ (see the text for the other model parameters). The dashed vertical lines limit the time interval where we plot the HIC and the HFC in Fig. 6.

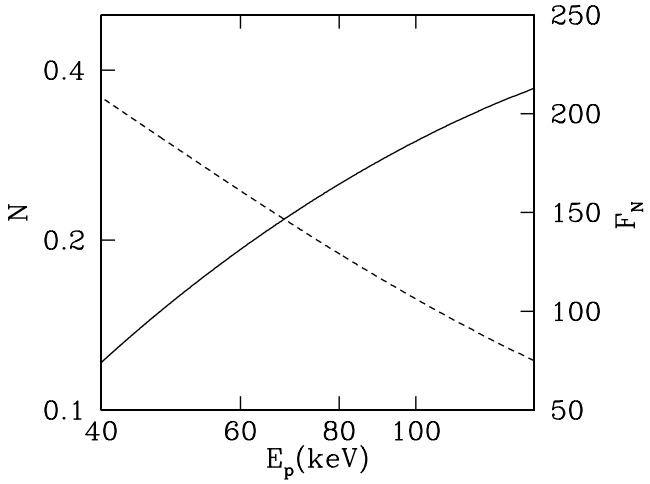

Figure 5. Hardness–intensity (full line) and hardness–fluence (dashed line) correlations for the pulse shown in Fig. 4.

The solution for $\dot{\mathcal{E}}$ including angular spreading has been obtained numerically and is also shown in Fig. 3. It differs from the analytical expression (equation 24) at early times but preserves the power-law decay of slope $\epsilon = 3/2$ at late times.

4 SPECTRAL EVOLUTION AND EMISSION PROCESSES

We now use the analytical model to follow the spectral evolution during pulse decay. If the dissipated energy is radiated by the synchrotron process the peak energy E_p is

$$E_\mathrm{p} = E_\mathrm{syn} \propto \Gamma B \Gamma_\mathrm{e}^2, \tag{27}$$

where B is the magnetic field and Γ_e is the characteristic electron Lorentz factor behind the shock. With classical equipartition assumptions B and Γ_e can be expressed as

$$B = \left(8\pi\alpha_\mathrm{B}\rho\epsilon c^2\right)^{1/2} \tag{28}$$

and

$$\Gamma_\mathrm{e} = \frac{\alpha_\mathrm{e}}{\zeta}\frac{m_\mathrm{p}}{m_\mathrm{e}}\epsilon, \tag{29}$$

where ρ is the density and ϵc^2 is the dissipated energy per unit mass (both in the comoving frame); α_B and α_e are the equipartition parameters and ζ is the fraction of electrons that are accelerated. Finally,

$$E_\mathrm{syn} \propto \Gamma \rho^{1/2} \epsilon^{5/2}, \tag{30}$$

where the comoving density ρ is proportional to r^{-2} (with r being the shock radius, $r \sim \Gamma^2 ct$) and ϵ is obtained from $\dot{\mathcal{E}} = \mathrm{d}M/\mathrm{d}t\,\Gamma\epsilon c^2$ and equation (16),

$$\epsilon = \frac{(1-\gamma)^2}{2\gamma}. \tag{31}$$

This leads to the following expression for E_syn:

$$E_\mathrm{syn} \propto \frac{(1-\gamma)^5}{\gamma^{7/2} t}, \tag{32}$$

which behaves as a power law ($E_\mathrm{p} \propto t^{-7/2}$) when $(1-\gamma) \sim t^{-1/2}$. This is much steeper than the observed spectral evolution of pulses, which satisfy both the HIC and the HFC. Instead of using equation (30) we therefore parametrize the peak energy with the more general phenomenological expression

$$E_\mathrm{p} \propto \Gamma \rho^x \epsilon^y \propto \frac{(1-\gamma)^{2y}}{\gamma^{4x+y-1} t^{2x}}, \tag{33}$$

which becomes

$$E_\mathrm{p} \propto \frac{1}{t^{2x+y}} \tag{34}$$

at late times. The exponents x and y can be different from their standard synchrotron values 1/2 and 5/2 if the equipartition parameters α_B, α_e or ζ vary with ρ or/and ϵ. For example, Daigne & Mochkovitch (1998) adopted a fraction ζ of accelerated electrons proportional to ϵ so that Γ_e remains constant, which leads to $x = y = 1/2$ and $E_\mathrm{p} \propto t^{-3/2}$. However, since most of the observed values of $\delta^\star = 2x + y$ are smaller than 1.5, it seems necessary to further reduce the x and y indices and we have therefore considered below the case $x = y = 1/4$, i.e. $\delta^\star = 0.75$.

5 TEMPORAL PROFILES

We obtain the temporal profile of synthetic pulses from equations (9), (24) and (33) of our model. We have represented in Fig. 4 a pulse formed when a wind of Lorentz factor $\Gamma_1 = 400$ and power $\dot{M}\Gamma_1 c^2 = 10^{52}$ erg s^{-1} is decelerated by a slow shell with $\Gamma_0 = 100$. We adopt $t_0 = 0.4$ s, $x = y = 1/4$ and $z = 1$. The profile is computed in the BATSE range (20–1000 keV) and the constant of proportionality in equation (33) is fixed to obtain a peak energy $E_\mathrm{p} = 300$ keV for the whole pulse spectrum. The pulse duration is close to 10 $(1 + z)$ t_0 as expected from the results obtained in Section 3.

The evolution after maximum is initially close to a $1/t$ decay (i.e. $n \sim 1$ in equation 6) as can be seen in Fig. 4, where $1/N(t)$ has also been represented. This can be simply understood from equation (14) which, for the decay slopes of the dissipated power $\epsilon = 1.5$ (equation 25) and of the peak energy $\delta^\star = 2x + y = 0.75$ gives

$$n = -0.75\zeta. \tag{35}$$

With $-2 \lesssim \zeta \lesssim -1$, the central value of n is indeed close to unity. Since the decay phase of our synthetic pulse can be described by equations (4) and (5) it should also satisfy both the HIC and the HFC. This is checked in Fig. 5 where the two relations have been

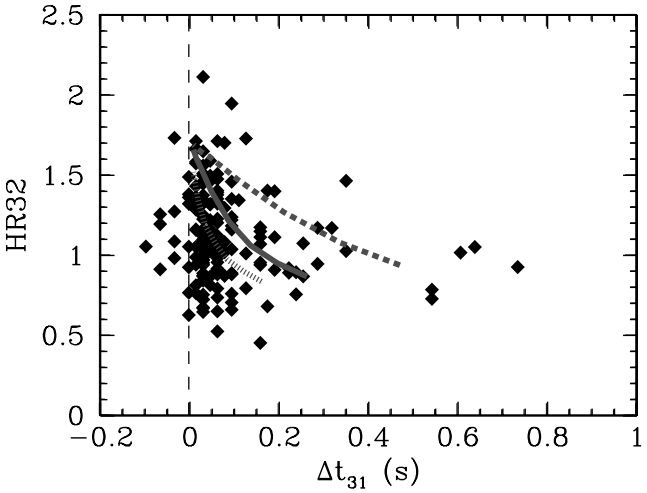

Figure 6. Time lag–hardness ratio diagram of BATSE bursts from Norris et al. (2000) compared with model predictions. The three lines represent sequences of synthetic pulses obtained with similar distributions of the Lorentz factor (the dotted line corresponds to $\Gamma_1 = 300$, the full line to $\Gamma_1 = 400$ and the dashed line to $\Gamma_1 = 600$; see the text for details).

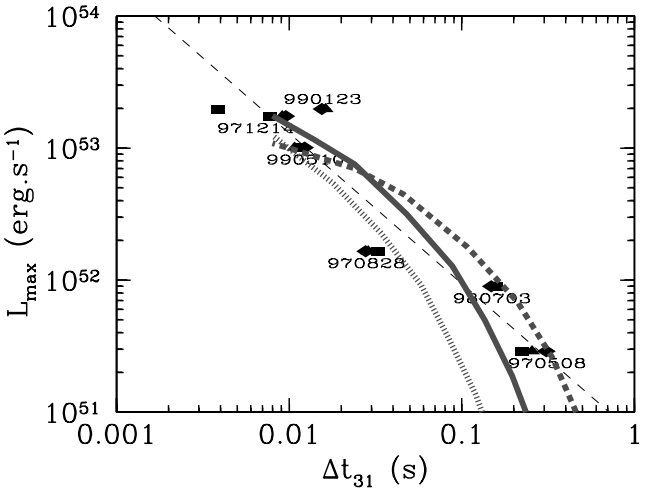

Figure 7. Time lag–luminosity correlation predicted by our model compared with Norris et al. (2000) results for six GRBs with known redshifts. The lines correspond to the three cases already considered in Fig. 6.

plotted in the time interval delimited by the two vertical lines in Fig. 4. The HIC is not a strict power law but its average slope $\delta \sim 0.9$ is in global agreement with the observations. The HFC is satisfied to a better accuracy since the relation between log E_p and the photon fluence is quasi-linear in the considered interval.

6 TIME LAGS

Norris et al. (2000) have shown that time-lags between different energy channels correlate with spectral hardness and possibly also with the burst peak luminosity. GRBs are distributed in a triangular domain of the time-lag–hardness ratio diagram (the hardest bursts having the shortest time-lags; see Fig. 6) and the time-lag–luminosity relation obtained from six bursts with known redshifts takes the form

$$L_{51} \simeq 130 \left(\frac{\Delta t_{31}}{0.01\ \mathrm{s}} \right)^{-1.14}, \tag{36}$$

where Δt_{31} is the time-lag between BATSE channels 3 and 1, and L_{51} is the luminosity in units of 10^{51} erg s^{-1}. In our model, we estimate time-lags by cross-correlating profiles in different energy channels obtained from equation (9). The first factor in equation (9) is

$$\psi(t) = \frac{F_\mathrm{E}(t)}{E_\mathrm{p}(t)}, \tag{37}$$

which behaves as $t^{2x+y-1.5}$ during pulse decay. The sign of $\Delta = 2x + y - 1.5$ is of great importance in determining the time t_max of maximum count rate and the related time-lags. If $\Delta < 0$ the function $\psi(t)$ has a maximum at some early time t_m before decreasing as t^Δ while it steadily increases for $\Delta > 0$. The second factor in equation (9) is $\varphi(E_\mathrm{p})$ so that t_max is the solution of the implicit equation

$$\frac{\dot{\psi}(t_\mathrm{max})}{\psi(t_\mathrm{max})} + \frac{\dot{E}_\mathrm{p}^\mathrm{max}}{E_\mathrm{p}^\mathrm{max}} \frac{\mathrm{d}\log\varphi}{\mathrm{d}\log E_\mathrm{p}}\bigg|_{E_\mathrm{p}^\mathrm{max}} = 0, \tag{38}$$

where $E_\mathrm{p}^\mathrm{max}$ and $\dot{E}_\mathrm{p}^\mathrm{max}$ are the values of E_p and its time derivative at $t = t_\mathrm{max}$. Since in most pulses the evolution of E_p precedes the count rate, $\dot{E}_\mathrm{p}^\mathrm{max}$ is negative. If the low-energy slope of the Band spectrum $\alpha \leqslant -1$, the derivative d log φ/d log $E_\mathrm{p}|_{E_\mathrm{p}^\mathrm{max}}$ is positive (see Fig. 1) and equation (38) then shows that $\dot{\psi}(t_\mathrm{max}) > 0$ which, for $\Delta < 0$, leads to

$$t_\mathrm{max} < t_\mathrm{m}, \tag{39}$$

which provides a strict upper limit on the time-lags between different energy channels

$$\Delta t < t_\mathrm{m}. \tag{40}$$

(If $\alpha > -1$, d log φ/d log $E_\mathrm{p}|_{E_\mathrm{p}^\mathrm{max}}$ can be weakly negative at large E_p but even in this case t_max never greatly exceeds t_m.)

When $\Delta \geqslant 0$, no constraint such as equation (40) applies and the time-lags can be quite large. Daigne & Mochkovitch (1998), who adopted $x = y = \frac{1}{2}$ ($\Delta = 0$), obtained lags of several seconds between BATSE channels 1 and 3 (or 4) for a pulse lasting approximately 10 s, while currently observed values are in the range 10^{-2} to a few 10^{-1} s. Moreover, for $\Delta > 0$ the time-lags increase with pulse hardness, in contradiction with the observations.

Conversely, with $x = y = \frac{1}{4}$ the time-lags are short ($\Delta t_{31} \lesssim 0.5$ s) even for long pulses and they decrease with increasing hardness. Fig. 6 shows the time-lag–hardness ratio relation given by our model superimposed to the Norris et al. (2000) results for BATSE bursts. The thick grey lines in Fig. 6 correspond to sequences of pulses of comparable duration ($t_{90} \sim 10$ s) obtained with similar distributions of the Lorentz factor (a slow shell with $\Gamma_0 = 100$ decelerating a fast wind with $\Gamma_1 = 300$, 400 or 600) and a varying value of the (isotropic) injected power (from 5×10^{51} to 10^{54} erg s^{-1}). Even if differences in duration and redshift will contribute to add scatter to their distribution it appears that synthetic pulses populate the same triangular domain as observed ones.

We finally checked whether our model was able to reproduce the time-lag–luminosity correlation (equation 36). When $x = y = 1/4$, we do find that the lags decrease with increasing luminosity. This is a consequence of the HIC and the time-lag–hardness ratio relation discussed above. The results are shown in Fig. 7 where the three lines correspond to the wind cases with $\Gamma_1 = 300$, 400 and 600 already considered in Fig. 6. It can be seen that there is an overall agreement between the model predictions and equation (36). However, at low luminosities and large time-lags we obtain a rather wide strip instead of a single relation such as equation (36). If this

is confirmed by the analysis of more GRBs with known redshifts, the time-lag–luminosity correlation will still be useful for statistical studies of large burst samples but may be quite inaccurate to estimate the luminosity of a specific event.

7 CONCLUSION

We have developed a simple model where GRB pulses are produced when a rapid part of a relativistic outflow is decelerated by a comparatively slower shell. We do not solve the true hydrodynamical problem but rather assume that the slow shell 'accretes' the fast moving material, which allows one to obtain an analytical solution for the dissipated power $\dot{\mathcal{E}}$. During pulse decay $\dot{\mathcal{E}} \propto t^{-3/2}$ as $\dot{\mathcal{E}} \propto t^{-3}$ when the evolution is fixed by shell geometry. To compute the spectral evolution of our synthetic pulses we parametrize the peak energy as $E_{\rm p} \propto \rho^x \epsilon^y \Gamma$, where ρ, $\epsilon\, c^2$ and Γ are, respectively, the post-shock values of the density, dissipated energy (per unit mass) and Lorentz factor. At late times, we obtain $E_{\rm p} \propto t^{-(2x+y)}$, which constraints x and y since in most observed bursts $E_{\rm p} \propto t^{-\delta^\star}$ with $\delta^\star \lesssim 1.5$. The synchrotron process with standard equipartition assumptions corresponds to $x = 1/2$ and $y = 5/2$ (i.e. $2x + y = 3.5$) and gives a much too steep spectral evolution. One has then to suppose that the equipartition parameters $\alpha_{\rm e}$, $\alpha_{\rm B}$ and ζ vary with ρ or/and ϵ to reduce x and y (a possible alternative being that energy is radiated by another process – different from the synchrotron one – but which can still be approximated by equation 33).

We have considered the case $x = y = 1/4$ and the resulting pulses then have temporal and spectral properties in excellent agreement with the observations. They follow both the HIC and the HFC during the decay phase and the time-lags between energy channels decrease with increasing pulse hardness and peak luminosity. We therefore conclude that if GRB pulses are produced by internal shocks, their temporal and spectral properties are probably governed by the hydrodynamics of the flow rather than by the geometry of the emitting shells.

REFERENCES

Band D. et al., 1993, ApJ, 413, 281
Daigne F., Mochkovitch R., 1998, MNRAS, 296, 275
Dermer C.D., Mitman K.E., 1999, ApJ, 513, L5
Fenimore E.E., Madras C.D., Nayakshin S., 1996, ApJ, 473, 998
Fishman G.J. et al., 1994, ApJS, 92, 229
Golenetskii S.V., Mazets E.P., Aptekar R.L., Ilinskii V.N., 1983, Nat, 306, 451
Granot J., Piran T., Sari R., 1999, ApJ, 513, 679
Kobayashi S., Piran T., Sari R., 1997, ApJ, 490, 92
Liang E., Kargatis V., 1996, Nat, 381, 49
Meszaros P., Rees M.J., 1993, ApJ, 405, 278
Norris J.P., Nemiroff R.J., Bonnell J.T., Scargle J.D., Kouveliotou C., Paciesas W.S., Meegan C.A., Fishman G.J., 1996, ApJ, 459, 393
Norris J.P., Marani G.F., Bonnell J.T., 2000, ApJ, 534, 248
Rees M.J., Meszaros P., 1994, ApJ, 430, L93
Ryde F., Svensson R., 2000, ApJ, 529, L13
Ryde F., Svensson R., 2002, ApJ, 566, 210
Soderberg A.M., Fenimore E.E., 2001, in Costa E., Frontera F., Hjorth J., eds, Gamma-ray Bursts in the Afterglow Era. Springer-Verlag, Berlin, p. 87

This paper has been typeset from a TEX/LATEX file prepared by the author.